J Nanostruct 16(4): 5498-5519, Autumn 2026

RESEARCH PAPER

# The Role of the Morphology and Dispersion of Cellulose-Derived Carbon Quantum Dots in Determining the Structural, Optical, and Thermal Properties of Polyamide Nanocomposites

*Fatima Hussein Abed* [1], *Ahmed M. Abbas* [1], *Munther Al-Shakban* [2*]

[1] *Department of Chemistry, College of Science, University of Misan, Misan, Iraq*

[2] *Department of Physics, College of Science, University of Misan, Misan, Iraq*

## ARTICLE INFO

***Article History:***
*Received 15 June 2026*
*Accepted 27 August 2026*
*Published 01 October 2026*

***Keywords:***
*Carbon Quantum Dots (CQDs)*
*Cellulose-Derived Carbon Dots*
*Fluorescence*
*Polyamide*
*Polymer Nanocomposites*
*Thermal Stability*

## ABSTRACT

Carbonaceous nanomaterial-containing polymer composites are promising systems for modifying the optical and thermal properties of polymers; however, their performance strongly depends on nanomaterial morphology, dispersion, and interfacial interactions with the polymer matrix. In this study, a series of polyamide polymers (A1–A3) was synthesized, and the corresponding NA1–NA3 composites were prepared by physical blending with a cellulose-derived carbonaceous nanomaterial. The chemical structures were characterized using FT-IR, $^{1}$H NMR, and $^{13}$C NMR spectroscopy, while XRD, FESEM, TEM, and EDX were employed to investigate the structural, morphological, and elemental characteristics. Optical and thermal properties were evaluated using UV–Vis, fluorescence spectroscopy, and TGA. FT-IR and NMR results supported the formation of the proposed polymeric structures, whereas FESEM revealed noticeable surface morphological changes after composite formation. TEM showed a heterogeneous morphology comprising needle- and rod-like structures with dense particle aggregates, indicating considerable agglomeration and particle overlap. Fluorescence measurements showed that emission intensity was strongly affected by the nature and aggregation state of the carbonaceous material, which limited the appearance of distinct fluorescence. TGA results revealed changes in the decomposition profiles and char residue percentages, although thermal stability was not consistently improved in all composites. Overall, the results demonstrate that the behavior of carbonaceous nanomaterials within polyamide matrices is governed by their morphology, dispersion, and interfacial interactions, which should be carefully controlled to improve composite performance.

**How to cite this article**
*Abed F., Abbas A., Al-Shakban M. The Role of the Morphology and Dispersion of Cellulose-Derived Carbon Quantum Dots in Determining the Structural, Optical, and Thermal Properties of Polyamide Nanocomposites. J Nanostruct, 2026; 16(4):5498-5519. DOI: 10.22052/JNS.2026.04.082*

## INTRODUCTION

Polyamides (PAs) are a class of high-performance polymers characterized by the presence of repeating amide linkages (–CONH–) within their molecular backbone. They may be naturally occurring, such as proteins, or synthetically produced, with nylon being the most widely known synthetic polyamide. Owing to the strong intermolecular hydrogen bonding between adjacent amide groups, polyamides exhibit excellent mechanical strength, thermal stability, wear resistance, chemical resistance, and good processability. These outstanding properties enable their reinforcement with fibers

* *Corresponding Author Email: Mundher.Al-Shakban@uomisan.edu.iq*

or nanoparticles to produce advanced composite materials with enhanced functional performance, allowing polyamides to replace conventional metallic materials in numerous engineering applications requiring lightweight and durable structures [1,2].

The importance of polyamides lies in their ability to maintain excellent mechanical performance under severe service conditions, including elevated temperatures, continuous mechanical stress, and exposure to aggressive chemical environments. Furthermore, their chemical structure allows easy modification and reinforcement with various nanomaterials, expanding their applications in high-performance engineering materials, electronics, biomedical devices, and sustainable technologies. These advantages continue to stimulate extensive research into the development of novel polyamide-based materials [3]. Polyamides can be synthesized using several polymerization techniques depending on the desired polymer structure and application. The most widely used industrial method is condensation polymerization, which involves the reaction of diamines with dicarboxylic acids or their derivatives, such as acid chlorides, to produce polyamide chains. Another important method is ring-opening polymerization (ROP) of cyclic lactams, particularly ε-caprolactam, for the production of Nylon 6. Other preparation techniques, including interfacial polymerization and solution polymerization, are employed to obtain specialty polyamides with tailored structures and enhanced properties for advanced technological applications [1,4].

Owing to their exceptional mechanical, thermal, and chemical properties, polyamides are extensively used in numerous industrial and commercial applications. They are widely employed in the automotive and aerospace industries, electrical and electronic components, textile fibers, packaging materials, engineering plastics, bearings, gears, and membrane technologies. In recent years, polyamide nanocomposites have attracted increasing attention for applications in water purification, biomedical devices, sensors, flexible electronics, and advanced functional materials due to their enhanced performance and multifunctional characteristics [5].

Composite materials are engineered by combining two or more constituents with different physical or chemical properties to obtain materials with superior performance compared to the individual components. They generally consist of a continuous matrix that binds and protects a reinforcing phase, which may be in the form of fibers, particles, or platelets. This combination enhances the mechanical, thermal, and electrical properties of the material, making composites widely used in aerospace, automotive, electronics, and biomedical applications. Recent advances in nanotechnology have further improved composite performance through the incorporation of nanoscale fillers [6]. Polymer nanocomposites (PNCs) are among the most advanced classes of functional materials, consisting of a polymer matrix reinforced with nanoscale fillers having at least one dimension within the range of 1–100 nm. Over the past two decades, these materials have attracted significant research interest because the incorporation of a small amount of nanofillers, such as carbon nanotubes, graphene, metal oxides, and carbon dots, can remarkably enhance the mechanical, thermal, electrical, optical, and barrier properties of polymer matrices. These improvements are mainly attributed to the high specific surface area of nanofillers and the strong interfacial interactions between the nanoparticles and polymer chains. Consequently, polymer nanocomposites have become promising materials for applications in sensing, electronics, water treatment, and biomedical technologies [7].

Carbon dots (CDs) are a new generation of carbon-based nanomaterials with a typical particle size below 10 nm. They have attracted considerable attention because of their unique combination of strong photoluminescence, excellent photostability, high chemical stability, low toxicity, good biocompatibility, and ease of surface functionalization. These outstanding properties have enabled their widespread use in sensing, bioimaging, chemical detection, and optoelectronic applications. Furthermore, the incorporation of carbon dots into polymer matrices has led to the development of advanced polymer nanocomposites with enhanced functional performance for a wide range of emerging technologies [8]. Carbon dots (CDs) can be synthesized through two main strategies: top-down and bottom-up approaches. Top-down methods involve breaking down bulk carbon materials, such as graphite, carbon nanotubes, and activated carbon, into nanosized particles using techniques including electrochemical oxidation, laser ablation, and chemical oxidation. In contrast,

bottom-up approaches produce carbon dots from small molecular precursors or organic compounds through hydrothermal, solvothermal, microwave-assisted, and pyrolysis methods. Among these strategies, bottom-up synthesis has become the most widely employed because of its simplicity, low cost, and excellent control over particle size, surface functional groups, and optical properties through careful selection of precursors and reaction conditions [9].

Due to their outstanding optical properties, excellent biocompatibility, and low toxicity, carbon dots (CDs) have been widely applied in chemical and biosensing, bioimaging, optoelectronic devices, photocatalysis, energy storage, water treatment, and as nanofillers for enhancing the mechanical, thermal, and optical properties of polymer nanocomposites. Their multifunctional characteristics have made them one of the most promising carbon-based nanomaterials for advanced technological applications [10].

Several studies have recently investigated the incorporation of carbon dots into polymer matrices to improve their multifunctional properties, Pandey et al. (2025) reviewed recent advances in polymer/carbon dot nanocomposites and discussed various fabrication techniques, including *in situ* polymerization, solution blending, melt blending, and surface functionalization of carbon dots to improve their compatibility with polymer matrices. The authors reported that incorporating carbon dots significantly enhanced the mechanical, thermal, electrical, and optical properties of polymer nanocomposites, leading to their widespread application in flexible electronics, sensing devices, energy storage, biomedical fields, and environmental remediation [11].

Although polymer/carbon dot composites have been extensively studied, their performance strongly depends on carbon dot morphology, dispersion, and interfacial interactions with the polymer matrix. Therefore, these factors were examined in the prepared TBT-based polyamide composites.

Based on the above discussion, the present study aimed to synthesize a series of TBT-based polyamide polymers and prepare their corresponding composites with cellulose-derived carbonaceous nanomaterials by physical blending. The prepared materials were characterized using FT-IR, $^{1}$H NMR, $^{13}$C NMR, XRD, FESEM, EDX, TEM, UV–Vis absorption spectroscopy, photoluminescence spectroscopy, and TGA to investigate the influence of nanomaterial incorporation on the chemical structure, morphology, optical behavior, and thermal decomposition characteristics of the polyamide matrices.

## MATERIALS AND METHODS

### *Materials*

Terephthalaldehyde (99.5%, Bide Pharm, China), thiosemicarbazide (98%, Loba Chemie Pvt. Ltd., India), absolute ethanol (99.9%, Fluka, Germany), phthaloyl chloride (99%, Aladdin, China), adipoyl chloride (98%, Pallav Chemicals & Solvents, India), sebacoyl chloride (95%, Macklin, China), and N,N-dimethylformamide (DMF, 99.97%, Fisher Scientific, United Kingdom) were used in the synthesis procedures. Hexane (99%, SRL, India) and ethyl acetate (99.5%, SRL, China) were employed for chromatographic monitoring and purification. Cellulose of high purity was supplied by Sigma–Aldrich, USA, and sodium hydroxide (NaOH) was used in the preparation of the cellulose-derived carbonaceous nanomaterial. Triethylamine was employed as an acid scavenger during polymerisation. All chemicals were used as received without further purification.

### *Instruments*

Fourier transform infrared (FT-IR) spectra were recorded over the range of 400–4000 $cm^{-1}$ using a Shimadzu FT-IR 8400S spectrophotometer (Shimadzu, Japan). The $^{1}$H and $^{13}$C NMR spectra were measured on a Bruker DMX-300 spectrometer (400 MHz, Bruker, Germany) using DMSO-$d_6$ as the solvent and tetramethylsilane (TMS) as the internal standard. Thermogravimetric analysis (TGA) was performed using an SDT-Q600 thermal analyzer (TA Instruments, USA) under a nitrogen atmosphere at a heating rate of 20 °C $min^{-1}$ over the temperature range of 25–800 °C. X-ray diffraction (XRD) patterns were obtained using a HAOYUAN Dx-2700BH diffractometer (Haoyuan, China) with Cu Kα radiation (λ = 1.5406 Å). The morphology of the samples was examined by field-emission scanning electron microscopy (FESEM) coupled with energy-dispersive X-ray spectroscopy (EDX) using a JEOL JSM-7600F microscope (JEOL, Japan). Transmission electron microscopy (TEM) images were recorded using a Tecnai G2 F20 microscope (FEI, USA). UV–visible absorption spectra were measured using a UV–Vis spectrophotometer, while photoluminescence (PL) spectra were

recorded using a fluorescence spectrophotometer equipped with a quartz cuvette. The electrical conductivity of the polymer films was determined using a four-point probe conductivity meter.

*Procedures*

*Synthesis of Schiff-base diamine monomer (TBT) 3.1*

Terephthaldehyde (1 mmol, 1.3422 g) was dissolved in ethanol under mild heating at 60 °C. Separately, thiosemicarbazide (2 mmol, 1.8231 g) was dissolved in an ethanol–water mixture (1:3, v/v). The thiosemicarbazide solution was gradually added to the aldehyde solution under continuous stirring, and the reaction mixture was refluxed for 5 h. The progress of the reaction was monitored by TLC using hexane: ethyl acetate (2:1) as the mobile phase. After completion, the mixture was cooled to room temperature, and the precipitated product was collected by filtration. The obtained solid was washed with a cold ethanol–water mixture (1:1, v/v) and dried in a vacuum oven to afford the final product as a yellow solid, with a melting point of 270–272 °C.

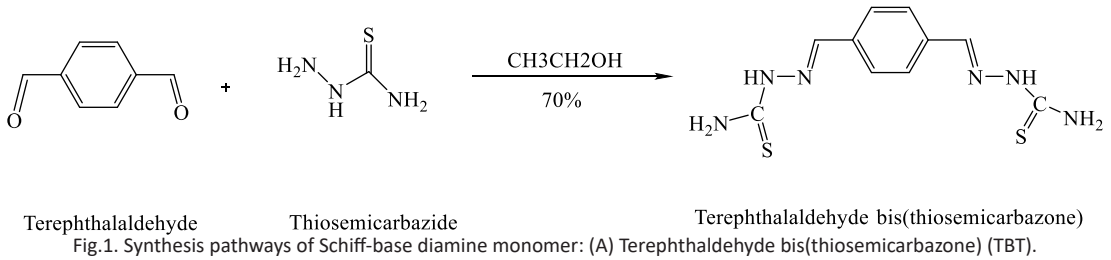


Fig.1. Synthesis pathways of Schiff-base diamine monomer: (A) Terephthaldehyde bis(thiosemicarbazone) (TBT).

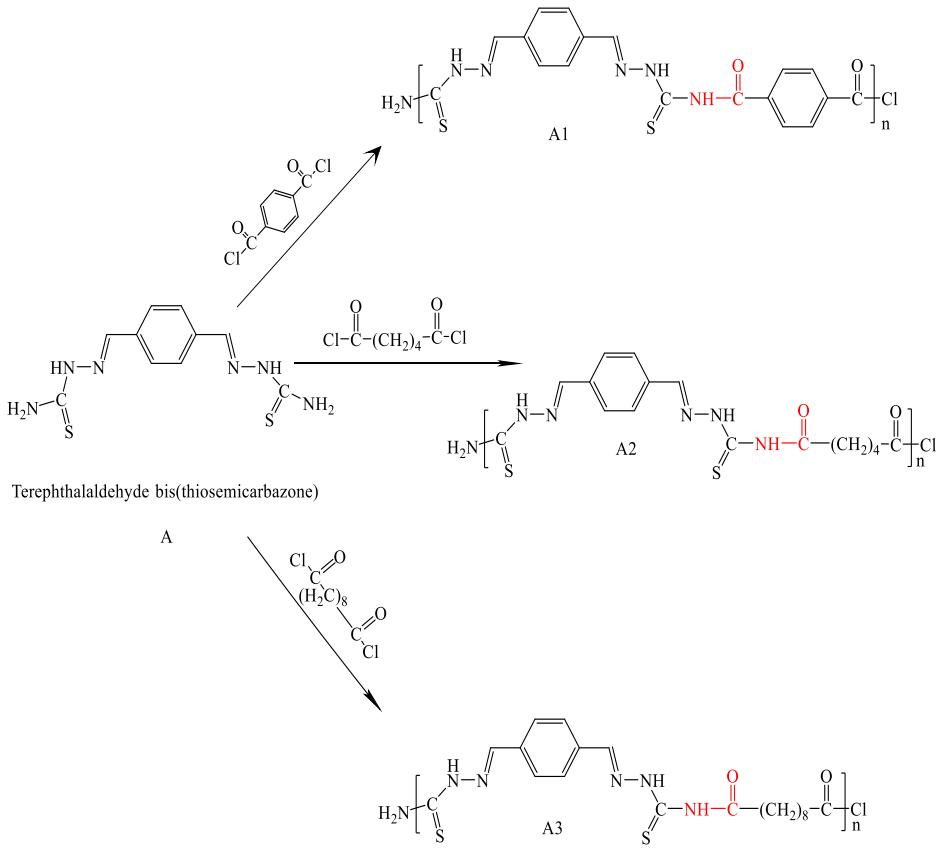


Fig. 2. Polycondensation route for polyamide polymers derived from monomer A(TBT).

*Polycondensation of TBT- based polyamide polymers*

Compound TBT *(5 mmol, 1.4009 g)* was dissolved in dry DMF (25 mL) in a three-necked round-bottom flask equipped with a magnetic stirrer. The reaction was carried out under a nitrogen atmosphere, and the reaction mixture was then cooled in an ice bath at 0 °C. A few drops of triethylamine (TEA) were added as an HCl scavenger.

Acid chloride (5 mmol) was added dropwise to the reaction mixture under continuous stirring while maintaining the temperature at 0 °C. After complete addition, the mixture was stirred at 0 °C for 1 h, then allowed to gradually reach room temperature and further stirred at 20 °C for 12 h.

After completion of the reaction, the reaction mixture was poured into cold distilled water to precipitate the product. The formed precipitate was collected by filtration, washed several times with distilled water, and dried in an vacuum oven to afford the desired product.

The resulting polyamide polymers were obtained as:

$A_1$: Off-white powder, m.p. 279-281, $A_2$: Yellow Powder, m.p. 239-241

$A_3$: Yellow Powder, m.p. 231-234.

*Synthesis of Carbon Quantum Dots (CQDs)*

Carbon quantum dots (CQDs) were prepared using cellulose as a carbon precursor. Briefly, 0.03 g of cellulose and 0.07 g of sodium hydroxide (NaOH) were dissolved in 10 mL of distilled water with continuous stirring until a homogeneous mixture was obtained. The resulting solution was then placed in a freezer overnight. After freezing, the mixture was allowed to return to room temperature and then subjected to sonication for 5 min to improve dispersion. Subsequently, the solution was irradiated in a microwave oven for

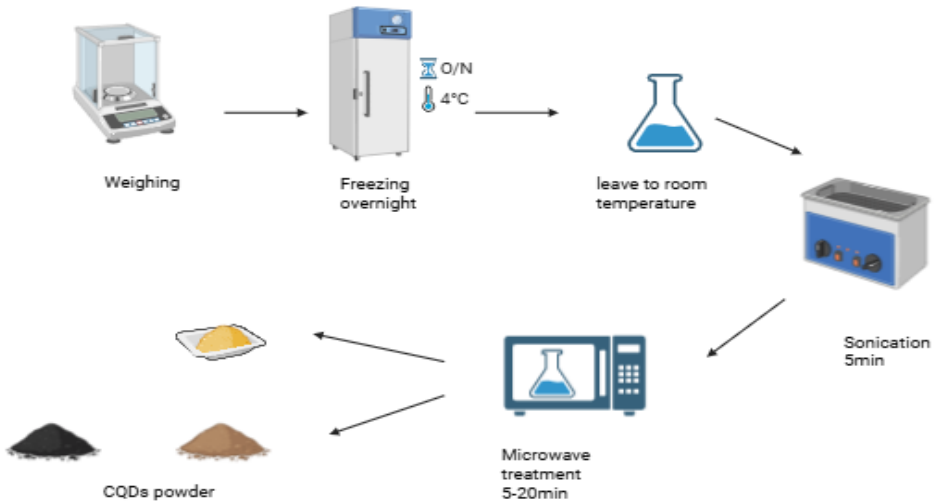


Fig. 3. Schematic illustration of the preparation of carbon quantum dots (CQDs) via alkaline freezing followed by microwave-assisted carbonization.

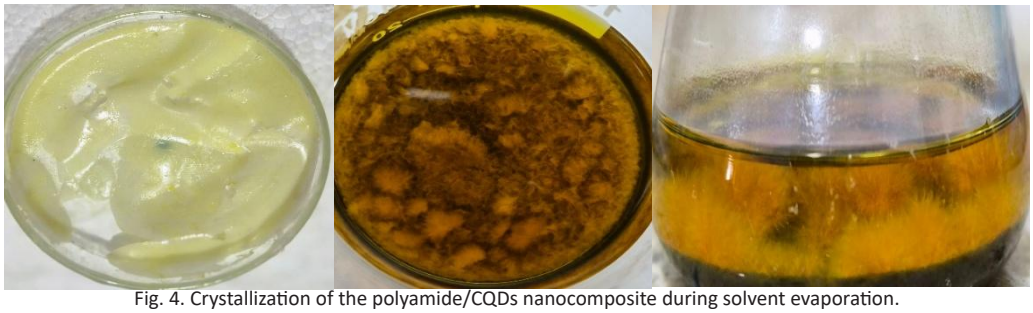

Fig. 4. Crystallization of the polyamide/CQDs nanocomposite during solvent evaporation.

5-20 min, during which the color of the solution gradually changed from pale yellow to dark brown/black, indicating the formation of carbon quantum dots.

*Preparation of Polyamide/CQDs Nanocomposite*

The polyamide/CQDs nanocomposites were prepared using the solution blending method at two different CQD loadings. For the first preparation, 0.5 g of the prepared polyamide and 0.5 g of CQDs were used at a weight ratio of 1:1 (w/w). For the second preparation, the CQD content was reduced to 2 wt% relative to the weight of the polyamide.

Initially, the required amount of polyamide was dissolved in N-methyl-2-pyrrolidone (NMP) under continuous stirring until a homogeneous polymer solution was obtained. Separately, the appropriate amount of CQDs for each composition was dispersed in NMP and subjected to sonication

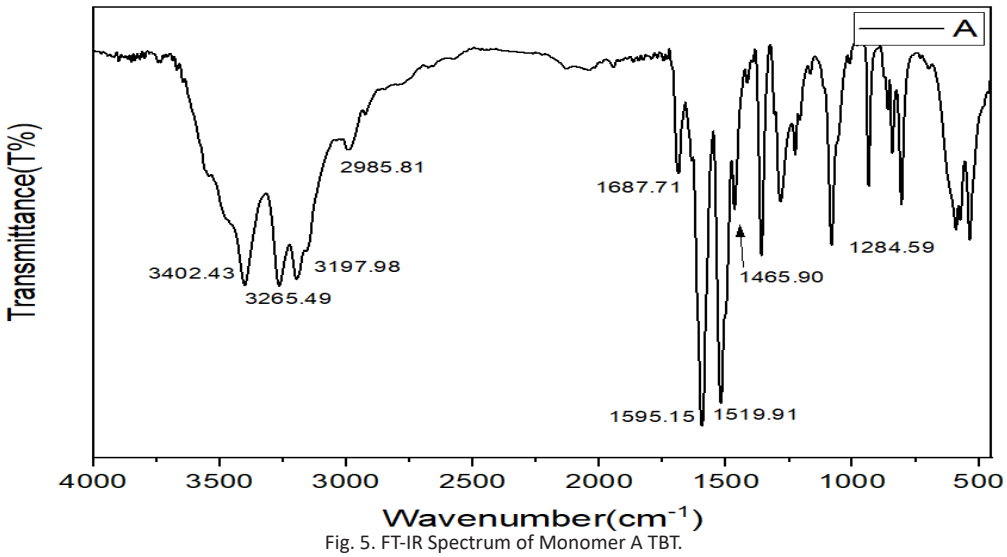


Fig. 5. FT-IR Spectrum of Monomer A TBT.

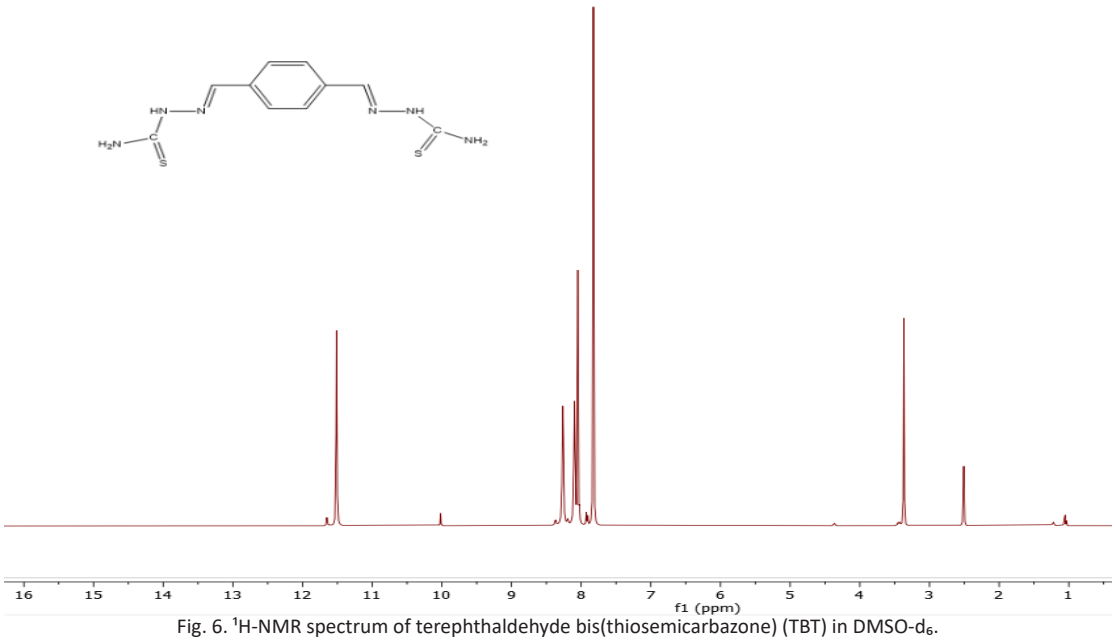


Fig. 6. $^{1}$H-NMR spectrum of terephthaldehyde bis(thiosemicarbazone) (TBT) in DMSO-$d_6$.

to improve their dispersion and reduce particle aggregation. The CQD dispersion was then gradually added to the polyamide solution under continuous stirring.

After complete addition, the resulting mixtures were further sonicated to promote the distribution of CQDs within the polyamide matrix. Finally, the prepared mixtures were cast onto clean glass plates and allowed to dry, yielding polyamide/CQD nanocomposites containing either 1:1 (w/w) polymer:CQDs or 2 wt% CQDs.

## RESULT AND DISCUSSION

*Characterization of diamine monomer Schiff base*

The FT-IR spectrum of monomer TBT showed characteristic absorption bands corresponding to its main functional groups. The broad bands observed at 3402.43 and 3265.49 $cm^{-1}$ were assigned to the asymmetric and symmetric N–H stretching vibrations of the $NH_2$ group, while the band at 3197.98 $cm^{-1}$ was attributed to N–H stretching. The bands at 2985.81 and 2926.01 $cm^{-1}$ were related to aromatic and aliphatic C–H stretching vibrations, respectively. The strong sharp band at 1595.13 $cm^{-1}$ was assigned to the azomethine C=N stretching vibration, whereas the band at 1519.91 $cm^{-1}$ was attributed to the aromatic C=C stretching vibration. In addition, the band at 1359.82 $cm^{-1}$ was assigned to C=S stretching, while the bands appearing in the range of 1465.90–1415.75 $cm^{-1}$ were related to C–N and N–N stretching vibrations. These results support the formation of the TBT monomer and confirm the presence of the thiosemicarbazone moiety in its structure.

Terephthaldehyde bis(thiosemicarbazone) (TBT), compound A, is shown in Fig. 6. The Spectrum was examined using $^1$H NMR (400 MHz, DMSO-d6); δ(ppm) = 8.04 (d, J = 8.2, 4H, Ar-H); 7.82 (s, 2H, $NH_2$); 8.26 (s, 1H, CH=N); and 11.50 (s,1H,NH) and The 13C-NMR (101 MHz, DMSO-d6). The existence of thiosemicarbazone functional groups, which can form hydrogen bonds with the polyamide matrix and contribute to backbone rigidity, is confirmed by the $^1$H NMR signals at δ 7.82 ($NH_2$) and 11.50 (NH). The development of the anticipated bis(thiosemicarbazone) structure is indicated by the CH=N signal at δ 8.26 ppm and the C=S signal at δ 177.78 ppm. A planar shape that is conducive to π-π interactions is suggested by aromatic carbon signals (δ 127–135 ppm) [12].

The incorporation of terephthalaldehyde bis(thiosemicarbazone) (TBT) into the polyamide structure is expected to influence the structural, thermal, and electrical behavior of the resulting polymers [13]. The thiosemicarbazone units contain polar thioamide groups, including –NH–C(=S)–NH– functionalities, which can participate in intra- and intermolecular hydrogen bonding. Such interactions may enhance chain packing, increase backbone rigidity, and restrict segmental mobility, thereby contributing to improved thermal stability. In addition, the aromatic terephthalaldehyde core and azomethine (C=N) linkages provide a conjugated and relatively planar framework, which may facilitate partial electron delocalization within the polymer structure [14]. The presence of nitrogen- and sulfur-containing groups can also improve interfacial interactions with incorporated nanofillers, supporting better filler dispersion and reducing agglomeration [15]. Consequently, the combined effects of hydrogen bonding, aromatic conjugation, chain rigidity, and filler–matrix interactions may explain the observed enhancement in the thermal and electrical properties of TBT-based polyamide nanocomposites.

*FT-IR spectra of polyamide polymers*

Fig. 7 presents a comparison of the FT-IR spectra of the synthesized polyamide polymers A1, A2, and A3. The FT-IR spectra of polymers A1, A2, and A3 prepared from the TBT monomer showed similar absorption features due to the presence of the same thiosemicarbazone-based structural unit, with differences related to the acid chloride segment incorporatedinto the polymer backbone.

The stretching vibration bands of $NH_2$ groups appeared within the region of 3424–3261 $cm^{-1}$, while the N–H stretching bands were observed at 3161, 3157, and 3155 $cm^{-1}$ for A1, A2, and A3, respectively. These bands are attributed to the amide/thioamide N–H groups. In this region, the aromatic C–H stretching vibrations may overlap with the broad N–H/$NH_2$ absorption bands, particularly due to hydrogen-bonding interactions; therefore, this region can be generally assigned to N–H/$NH_2$ stretching vibrations with possible contribution from aromatic C–H stretching.

The aliphatic C–H stretching vibrations appeared within the region of 3005–2823 $cm^{-1}$, corresponding to methylene groups or aliphatic segments present in the compounds. The carbonyl C=O stretching bands were recorded at 1595 $cm^{-1}$

for A1, 1693 $cm^{-1}$ for A2, and within the range of 1700–1690 $cm^{-1}$ for A3. These bands are attributed to C=O stretching vibrations, and the variation in their positions may be related to differences in the neighboring groups, hydrogen-bonding effects, or possible overlap with other vibrations in the structures.

The azomethine C=N stretching bands appeared at 1535, 1593, and 1635 $cm^{-1}$ for A1, A2, and A3, respectively, supporting the presence of C=N linkages in the structures. In addition, the C=C stretching vibrations were observed at 1519 $cm^{-1}$ for A1, 1500 $cm^{-1}$ for A2, and 1595 $cm^{-1}$ for A3, which are attributed to aromatic ring vibrations or conjugated double bonds within the molecular framework.

The thioamide C=S absorption bands appeared within the region of 1298–1224 $cm^{-1}$. These bands were observed at 1288–1224 $cm^{-1}$ for A1, 1280 $cm^{-1}$ for A2, and 1298–1238 $cm^{-1}$ for A3, and were assigned to C=S stretching coupled with C–N vibration within the thioamide group. Furthermore, the C–N stretching bands appeared at 1465, 1531, and 1525 $cm^{-1}$ for A1, A2, and A3, respectively, supporting the presence of C–N bonds in the synthesized compounds.

Accordingly, the appearance of the characteristic absorption bands corresponding to $NH_2$, N–H, aliphatic C–H, C=O, C=N, C=C, C=S, and C–N supports the proposed structures of compounds A1–A3 [16–18].

*Characterization of Nano Carbon Quantum Dots*

*FT-IR Analysis*

As shown in Fig. 8a, the FT-IR spectrum of sample C, prepared at a treatment time of 5 min, exhibited a broad absorption band at approximately 3441 $cm^{-1}$, attributed to the O–H stretching vibrations of surface hydroxyl groups. The bands observed at 2924 and 2854 $cm^{-1}$ are assigned to aliphatic C–H stretching vibrations, while the distinct band at approximately 1718 $cm^{-1}$ is attributed to C=O stretching vibrations of carbonyl and/or carboxyl groups. Furthermore, the bands at approximately 1626 and 1599 $cm^{-1}$ can be associated with C=C stretching vibrations within conjugated carbon domains. The intense absorption at approximately 1437 $cm^{-1}$ may be related to C–O–H deformation and/or vibrations of the carbon framework, whereas the bands in the 1100–1024 $cm^{-1}$ region are mainly attributed to C–O and C–O–C stretching vibrations, indicating the presence of oxygen-containing functional groups on the carbon surface.

In comparison, the FT-IR spectrum of sample N, prepared for 20 min (Fig. 8b), displayed a broad O–H absorption band at approximately 3408 $cm^{-1}$, together with C–H stretching bands at approximately 2955, 2922, and 2851 $cm^{-1}$. A band was also observed in the carbonyl/

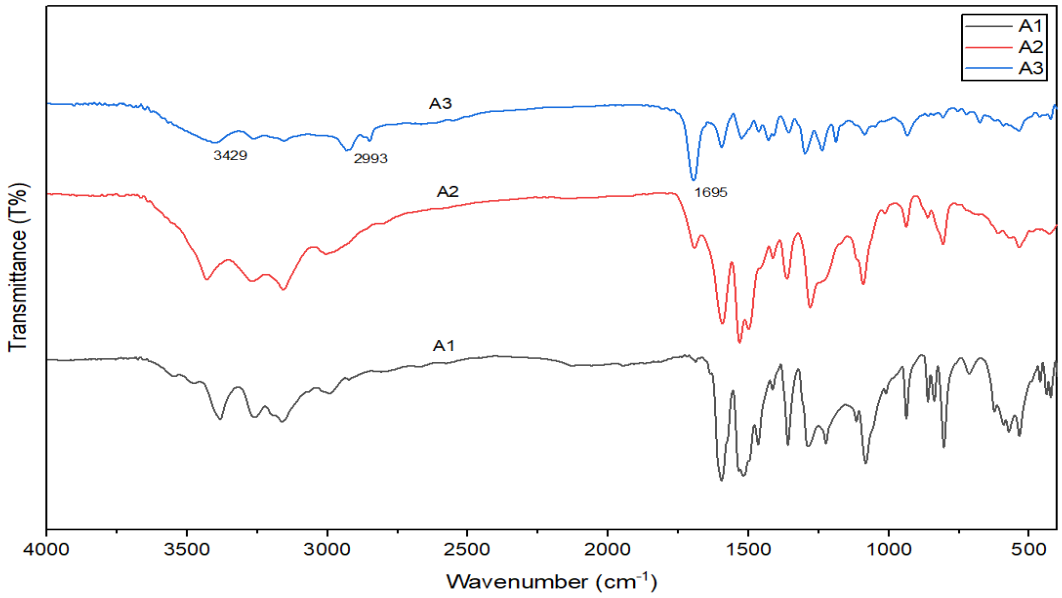


Fig. 7. FT-IR Spectrum of Polyamide Polymers.

conjugated region at approximately 1698 $cm^{-1}$, while additional prominent absorptions appeared at approximately 1435, 1161, and 1045 $cm^{-1}$. Comparison of Figs. 7a and 7b demonstrates that both carbon samples contain oxygen-bearing surface functionalities; however, noticeable changes in the position and relative appearance of the C=O- and C–O-related absorption bands occur with increasing treatment time. In particular, the relatively distinct C=O band at 1718 $cm^{-1}$ in C (5 min) indicates greater preservation of carbonyl-containing surface functionalities at the shorter treatment time. The spectral changes observed for N (20 min) are consistent with modification of the surface chemical environment during prolonged treatment, which may involve further dehydration, condensation, and carbonization. Thus, the comparison presented in Fig. 7 indicates that treatment time influences the surface functional groups and carbonization state of the resulting carbon materials, factors that may contribute to the differences observed in their fluorescence behavior [19–22].

The FT-IR spectra of the A-series polymers (A1–A3) before doping showed broad absorption bands in the region of approximately 3429–3157 $cm^{-1}$, which are attributed to the stretching vibrations of N–H groups belonging to amide and thioamide moieties, with possible partial overlap from aromatic C–H vibrations. Bands appearing in the region of 2993–2823 $cm^{-1}$ are assigned to aliphatic C–H stretching vibrations. The bands observed around 1695–1683 $cm^{-1}$ are attributed to amide C=O stretching, whereas the bands in the region of 1605–1505 $cm^{-1}$ are related to C=N, aromatic C=C, and C–N/amide II vibrations. In addition, the bands appearing in the region of 1298–1224 $cm^{-1}$ are assigned to thioamide/C=S vibrations with contribution from C–N, while the bands around 1115–1014 $cm^{-1}$ correspond to Ar–O–C / C–O–C stretching vibrations. In general, these absorption bands confirm the formation of

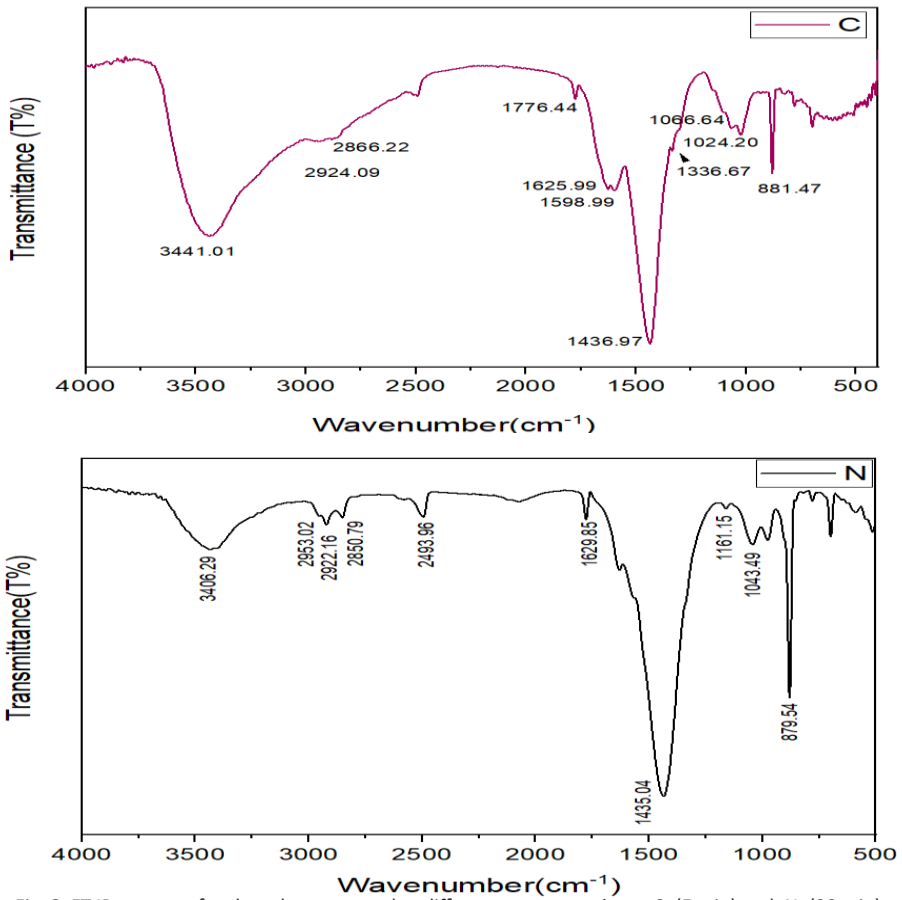


Fig. 8. FT-IR spectra of carbon dots prepared at different treatment times, C: (5 min) and, N: (20 min).

the prepared polymers and the presence of their main functional groups.

The FT-IR spectrum of the carbon quantum dots (N) showed a broad band at about 3406 $cm^{-1}$ attributed to surface O–H stretching, together with aliphatic C–H bands at 2953–2850 $cm^{-1}$, a characteristic C=O band at 1776 $cm^{-1}$, and additional bands at 1629 $cm^{-1}$ and 1161–1043

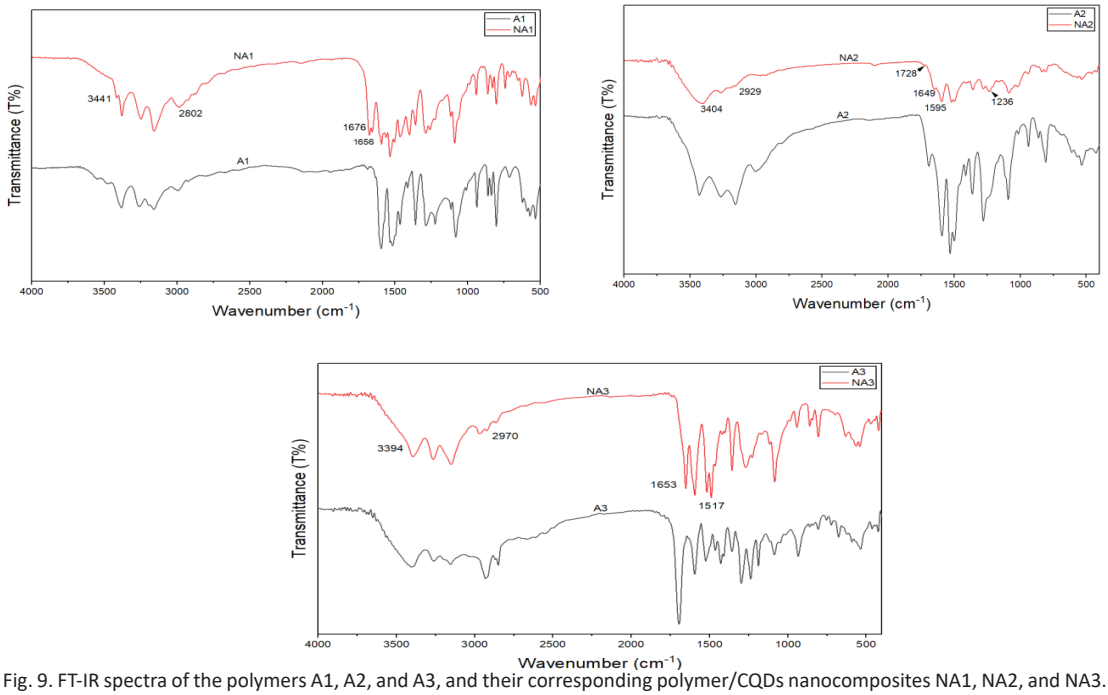


Fig. 9. FT-IR spectra of the polymers A1, A2, and A3, and their corresponding polymer/CQDs nanocomposites NA1, NA2, and NA3.

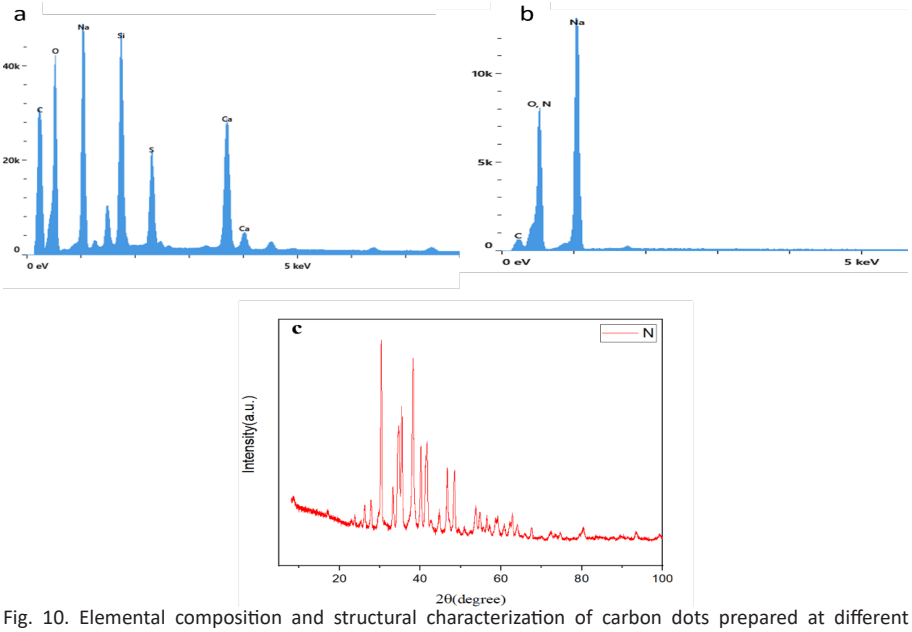


Fig. 10. Elemental composition and structural characterization of carbon dots prepared at different treatment times: (a) EDX spectrum of CQDs prepared for 20 min, (b) EDX spectrum of CQDs prepared for 5 min, and (c) XRD pattern of the carbonaceous nanomaterial.

$cm^{-1}$ assigned to C=C and C–O/C–O–C vibrations, indicating the presence of oxygen-containing surface groups on the CQDs. After doping the polymers and forming the composites NA1–NA3, broad bands appeared in the region of 3414–3151 $cm^{-1}$ due to the overlap of the polymer N–H vibrations with the surface O–H vibrations of the carbon quantum dots. A noticeable change was also observed in the carbonyl region, where the characteristic CQD band at 1776 $cm^{-1}$ no longer appeared in the same form; instead, shifted or merged bands were observed in the region of 1728–1653 $cm^{-1}$ in the composites, suggesting interactions between the oxygen-containing surface groups of the CQDs and the N–H or C=O groups of the polymer. Moreover, the persistence of bands in the region of 1562–1411 $cm^{-1}$ indicates that the C=N, C=C, and C–N vibrations of the polymer backbone were retained, meaning that the main polymer structure remained essentially unchanged after doping. The bands in the region of 1176–1085 $cm^{-1}$ became more pronounced in the composites, which can be attributed to the contribution of C–O and C–O–C groups from the carbon quantum dots. Therefore, the FT-IR results support the successful incorporation of carbon quantum dots into polymers A1–A3, leading to the formation of NA1–NA3 composites through physical interactions and hydrogen bonding without significant alteration of the main polymer structure [23].

*XRD and EDX Analysis*

As shown in Fig. 10, the XRD pattern of the prepared carbonaceous material exhibited a broad diffraction band centred at 2θ ≈ 20–30°, indicating its predominantly amorphous or poorly crystalline structure. This broad band is attributed

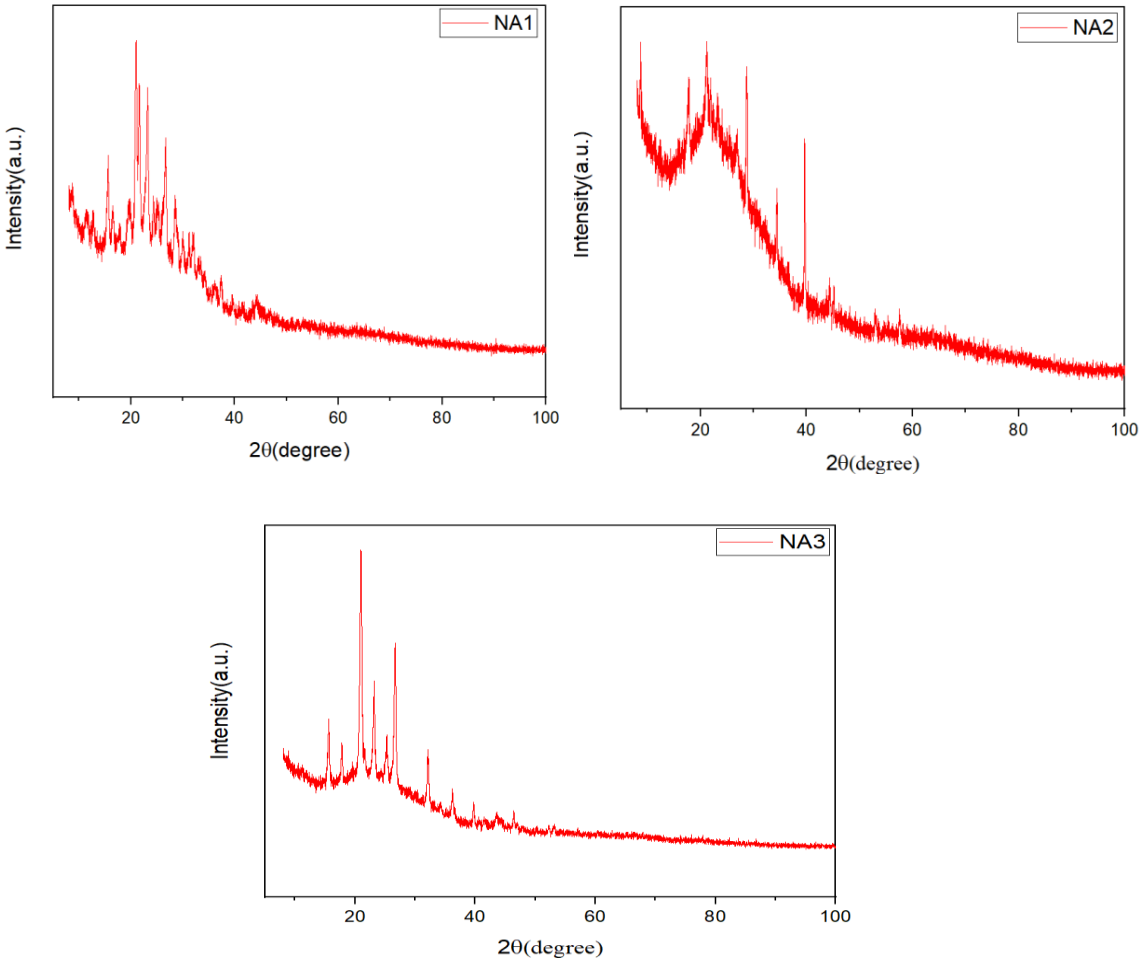


Fig. 11. XRD for a; NA1 Composite, NA2 Composite and NA3 Composite

to the (002) plane of graphitic-like carbon, which is characteristic of carbon-based nanomaterials. In addition, several sharp diffraction peaks were observed, suggesting the presence of residual inorganic crystalline species originating from the preparation process.

The EDX analysis revealed a pronounced difference in the elemental composition of the carbon dots prepared at different treatment times, as shown in Fig. 10a and Fig. 10b. The CQDs prepared for 20 min (Fig. 10a) exhibited a relatively high carbon content of 46.3 at.%, together with 34.4 at.% oxygen and 9.8 at.% sodium, indicating a greater extent of carbonization and the development of a more carbon-rich structure with prolonged treatment. In contrast, the CQDs prepared for 5 min (Fig. 10b) showed a lower carbon content of 9.9 at.%, accompanied by relatively high oxygen and nitrogen contents of 47.1 and 10.5 at.%, respectively, as well as 32.4 at.% sodium. These results suggest that the shorter preparation time preserves a higher proportion of O- and N-containing surface species, whereas prolonged treatment promotes carbonization and the partial loss of heteroatom-containing surface species. This trend is consistent with the FT-IR results, which indicated changes in the contribution of surface functional groups with increasing carbonization time, and also supports the observed difference in fluorescence behavior. The 5-min sample exhibited stronger fluorescence, whereas the fluorescence was markedly reduced in the 20-min sample. The relatively high abundance of oxygen- and nitrogen-containing surface species in the shorter-time sample may contribute to emissive surface states, while prolonged carbonization can increase structural condensation and reduce some of these surface states, thereby contributing to fluorescence quenching. The minor elements detected in the 20-min sample, including Al, Si, S, Ca, Ti, and Ni, may originate from trace impurities or sample/substrate-related contributions during EDX analysis and therefore should not be directly assigned to the intrinsic CQD structure without additional characterization [24–26].

Fig. 11 presents the X-ray diffraction patterns

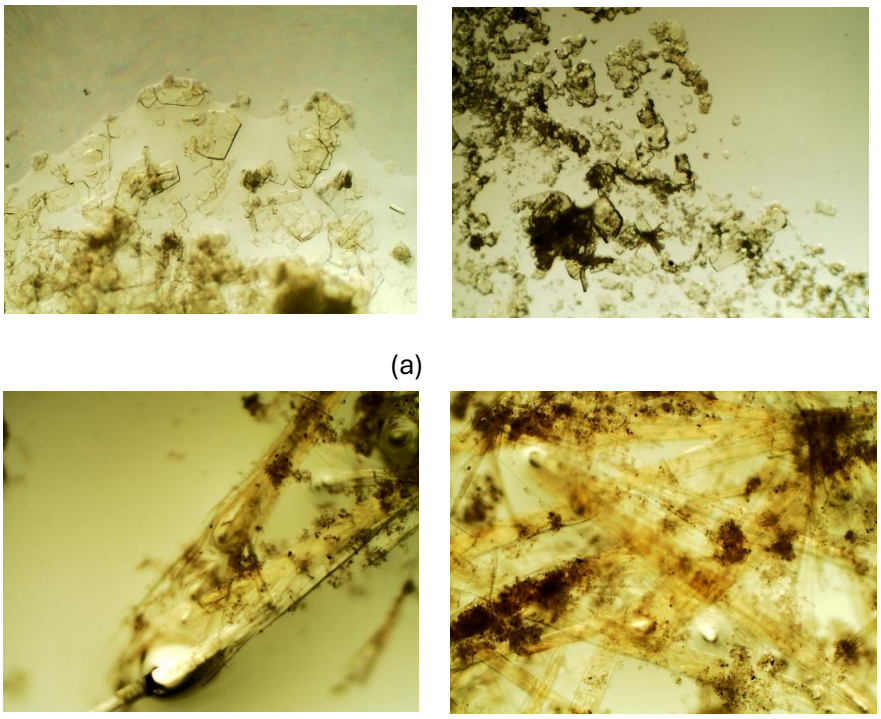


Fig. 12. Optical micrographs showing the morphological characteristics of (a) pristine polyamide(A) and (b) polyamide/CQDs nanocomposite (NA1).

of the NA1, NA2, and NA3 polymer/carbonaceous nanomaterial composites, allowing comparison of their structural characteristics and diffraction behaviour.The X-ray diffraction patterns of the prepared polymer/CQDs nanocomposites, NA1, NA2, and NA3, exhibited broad diffraction backgrounds accompanied by several diffraction peaks, indicating an amorphous to semi-crystalline structure. The broad diffraction feature observed around may be attributed to the disordered carbon structure and graphitic-like domains of carbon quantum dots, which are commonly reported for CQDs [27]. In comparison with the CQDs sample N, the diffraction peaks in NA1–NA3 appeared less distinct and overlapped with the broad polymer-related background, suggesting the incorporation of CQDs within the polymer matrix. The presence of diffraction peaks in the nanocomposites also indicates the existence of locally ordered regions, with NA3 showing relatively sharper peaks than NA1 and NA2, suggesting a higher degree of local ordering or a different CQDs distribution within the polymer matrix [28]. Since the XRD pattern of the pristine polymer was not recorded, the structural interpretation was based on the comparison between the nanocomposites and the CQDs pattern only, and changes relative to the neat polymer cannot be directly confirmed.

*Optical Microscopy Analysis*

Fig. 12 presents the optical microscopy images of the pristine polyamide (A1) and the corresponding polyamide/CQDs nanocomposite (NA1), highlighting the morphological changes resulting from the incorporation of carbon quantum dots.

The optical microscopy images revealed a clear difference between the pristine polyamide and

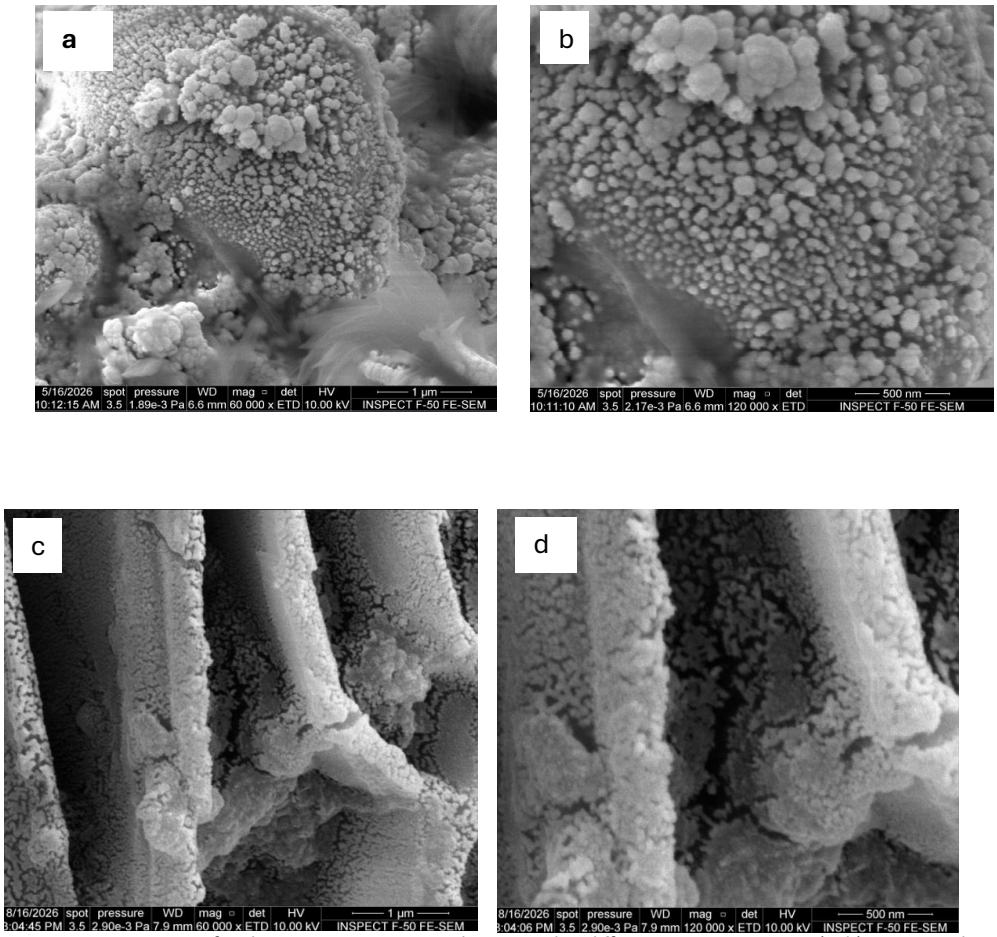


Fig. 13. FESEM images of carbonaceous nanomaterials prepared at different treatment times: (a, b) 20 min and (c, d) 5 min.

the NA1 nanocomposite. The pristine polyamide exhibited relatively large plate-like and needle-like crystals, indicating well-developed crystalline regions within the polymer matrix. In contrast, the NA1 nanocomposite showed noticeable changes in crystal morphology, where the crystals became less regular and more interconnected, accompanied by the appearance of dark domains distributed on the crystal surfaces and within the intercrystalline regions. These morphological changes may be attributed to the incorporation of carbon quantum dots (CQDs), which could act as heterogeneous nucleation sites and influence the crystal growth and distribution within the polyamide matrix. Furthermore, the dark domains may indicate the presence of nanofiller agglomerates resulting from incomplete dispersion within the polymer matrix. Overall, these observations suggest that the incorporation of CQDs altered the morphological characteristics of the polyamide and provided evidence for the successful formation of the nanocomposite.

*FESEM Analysis*

The FESEM images in Fig. 13 demonstrate the effect of preparation time on the morphology of the carbonaceous samples. The 20-min sample (Fig. 13a and Fig. 13b) exhibited dense aggregates of quasi-spherical features with a rough surface, suggesting increased carbonization and aggregation of the carbonaceous structures with prolonged treatment. In contrast, the 5-min sample (Fig. 13c and Fig. 13d) showed irregular and aggregated carbonaceous structures with a distinctly different morphology from the 20-min sample. This morphological difference is consistent with the EDX and FT-IR results, supporting changes in the degree of carbonization

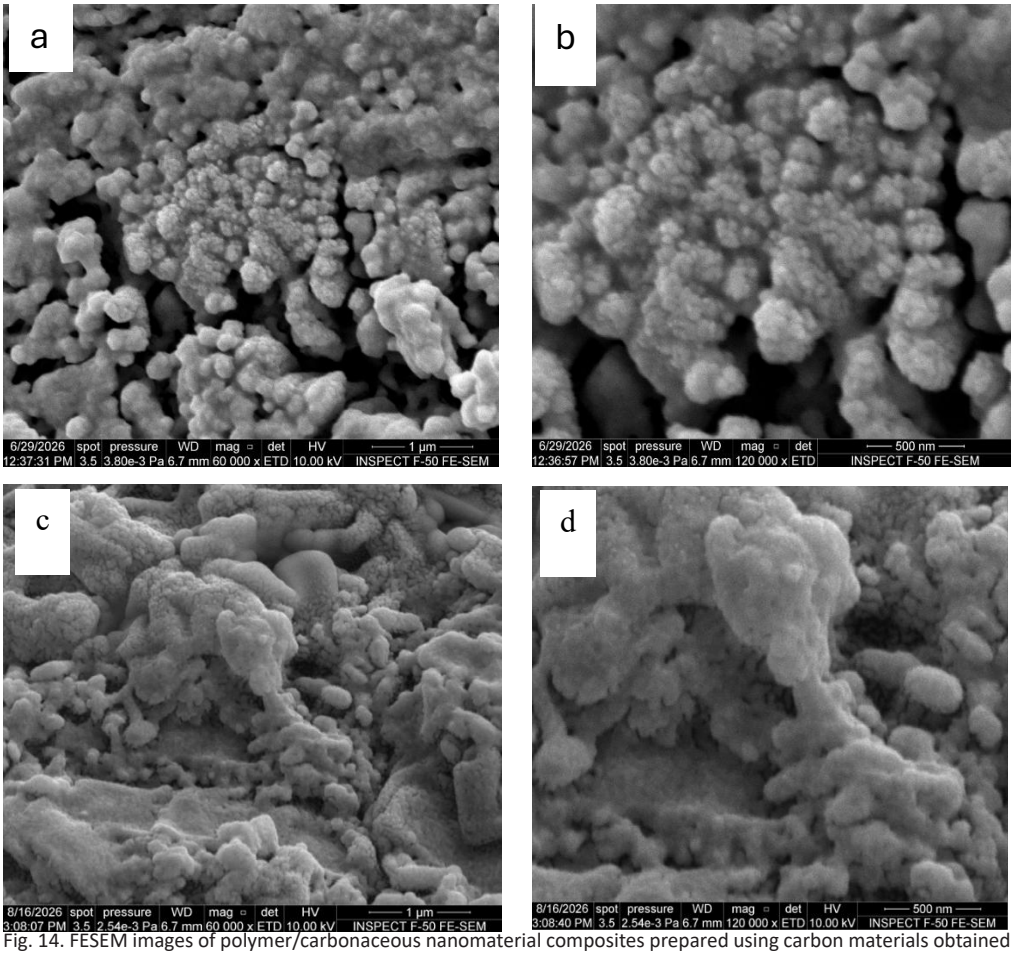


Fig. 14. FESEM images of polymer/carbonaceous nanomaterial composites prepared using carbon materials obtained at different treatment times: (a, b) 20 min and (c, d) 5 min.

and surface structure with increasing preparation time, which may contribute to the pronounced reduction in fluorescence observed for the 20-min sample [27,28].

The FESEM images in Fig. 14 demonstrate the effect of carbon preparation time on the morphology of the composites. The composite containing carbon prepared for 20 min (Fig. 14a and Fig. 14b) exhibited pronounced and dense aggregation of carbonaceous structures within/on the polymer matrix. In contrast, the composite containing carbon prepared for 5 min (Fig. 14c and Fig. 14d) showed a different morphology characterized by irregular aggregated structures associated with the polymer surface. The morphological differences between the two composites indicate that the preparation time of the carbonaceous material influences its interaction and distribution within the polymer matrix, which, together with differences in carbonization degree and surface chemistry, may contribute to the different fluorescence behavior of the two composites [28].

*TEM Analysis*

As shown in Fig. 15, the TEM images of the prepared carbon quantum dots (CQDs) at different magnifications provide detailed information about their morphology, particle shape, and aggregation state,The TEM images revealed that the prepared sample possesses a highly heterogeneous morphology consisting of elongated needle- and rod-like structures together with dense, irregular aggregates of fine particles. Considerable particle overlap and the formation of dark, electron-dense domains were also observed, indicating pronounced agglomeration rather than the formation of discrete and uniformly distributed spherical nanoparticles. The needle- and sheet-like structures may be attributed to crystalline or semi-crystalline phases, residual precursor materials, or secondary products formed during synthesis or drying on the TEM grid. Such extensive agglomeration and morphological heterogeneity

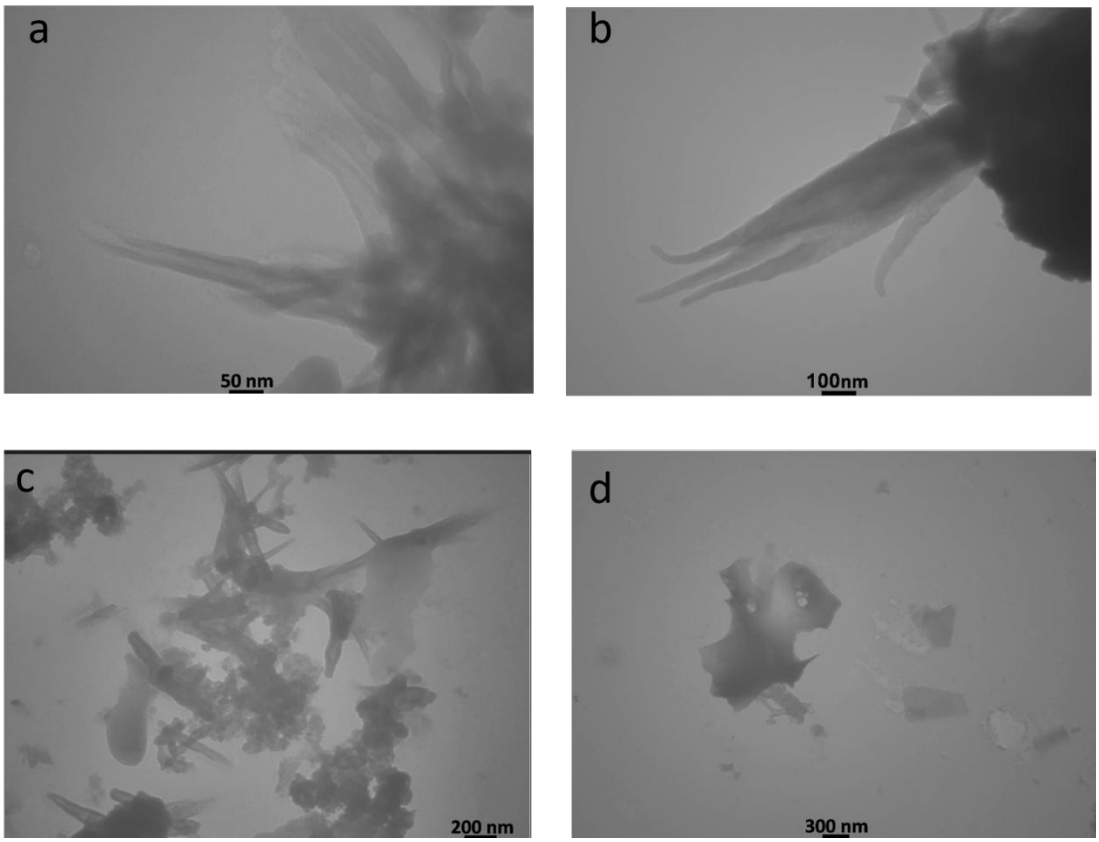


Fig. 15. TEM images of the prepared carbon quantum dots (CQDs) at different magnifications, with scale bars of a)50, b)100, c)200, and d) 300 nm.

may explain the weak or absent fluorescence of the sample. Close contact between the potential emissive centres can enhance interparticle interactions and promote non-radiative energy dissipation, resulting in aggregation-caused fluorescence quenching. Moreover, the formation of large carbonaceous domains or non-emissive phases may increase excitation-light absorption while reducing emission efficiency. Therefore, the TEM results suggest that the lack of fluorescence may not be related solely to surface chemistry, but also to severe aggregation, irregular particle morphology, broad size variation, and the absence of clearly resolved, discrete spherical carbon dots [29].

The TEM images revealed pronounced aggregation and overlapping of the nanostructures, which may directly contribute to the weak or absent fluorescence of the prepared sample. Close contact between carbon dots in the aggregated or solid state is known to enhance π–π interactions and coupling between emissive centres, thereby promoting non-radiative relaxation pathways and causing aggregation-caused quenching. The presence of dense, dark carbonaceous domains may also reduce the observed fluorescence by absorbing the excitation light or reabsorbing the emitted radiation through the inner-filter effect. In addition, the photoluminescence of carbon dots strongly depends on the formation of emissive surface states and molecular fluorophores during synthesis. Therefore, insufficient surface passivation, excessive carbonisation, or the presence of residual impurities and metal ions may create additional electron-transfer and non-radiative energy-loss pathways. Accordingly, the absence of detectable fluorescence in the present sample may be attributed to the combined effects of severe aggregation, morphological heterogeneity, light reabsorption, and an insufficient population of effective emissive surface states [30,31].

*Fluorescence Behavior of Cellulose-Derived Carbon Quantum Dots*

As shown in Fig. 16, the fluorescence behaviour of the cellulose-derived carbon quantum dots (CQDs) prepared at different reaction times was investigated using fluorescence spectroscopy, together with digital photographs under visible and UV light,The fluorescence emission spectra of the cellulose-derived CQDs prepared at different reaction times showed a clear dependence of emission intensity on the preparation time. The sample prepared at 5 min exhibited the strongest and broadest emission band in the blue–green region, with maximum emission around 450–480 nm, indicating the formation of highly emissive CQDs with active surface states. With increasing reaction time, the emission intensity decreased noticeably. The samples prepared at 8 and 10 min still showed fluorescence emission, but with lower intensity compared with the 5 min sample, while the 6 min sample exhibited very weak emission. This variation may be related to differences in carbonization degree, particle dispersion, and the formation of surface emissive centers during the early stages of CQDs formation [32].

fluorescence results indicate that a shorter

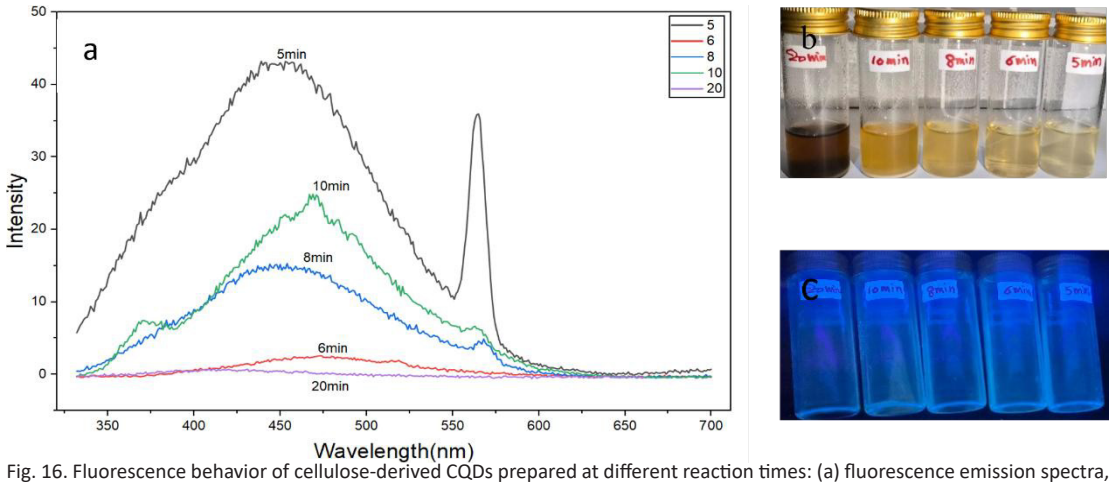


Fig. 16. Fluorescence behavior of cellulose-derived CQDs prepared at different reaction times: (a) fluorescence emission spectra, (b) digital photographs under visible light, and (c) photographs under UV irradiation.

preparation time, particularly 5 min, is more At longer preparation time, especially 20 min, the fluorescence was strongly quenched and almost disappeared. This behavior can be attributed to excessive carbonization, possible particle growth and aggregation, which reduce the number of effective emissive surface states and enhance non-radiative relaxation pathways. Therefore, the suitable for obtaining fluorescent CQDs, whereas prolonged reaction time leads to highly carbonized carbonaceous particles with weak or quenched fluorescence [33].

The sharp narrow signal observed around 560–570 nm is not considered as the main fluorescence emission band, because CQDs usually show broad emission bands; therefore, it may be related to instrumental scattering or a second-order excitation effect.

This behavior was further supported by the digital photographs of the CQDs samples under visible and UV light. Under visible light, the color of the samples gradually changed from yellow/brown to darker brown or black with increasing reaction time, indicating a higher degree of carbonization. Under UV irradiation, the samples prepared at shorter reaction times showed clearer blue emission, while the fluorescence became weaker at longer reaction times. This visual observation is consistent with the fluorescence spectra, confirming that prolonged reaction time leads to reduced fluorescence intensity due to over-carbonization and possible particle aggregation [34].

The neat A1 polymer exhibited very low fluorescence intensity and no distinct emission band within the investigated wavelength range, indicating that the polymer itself has no significant intrinsic fluorescence under the applied measurement conditions. The previously prepared NA1 composite, obtained by physical mixing at a 1:1 polymer-to-carbon ratio using carbon prepared for 20 min, showed only a weak and broad emission band approximately in the 430–520 nm region. The low fluorescence intensity of this sample may be attributed to the very high carbon loading, which increases the probability of

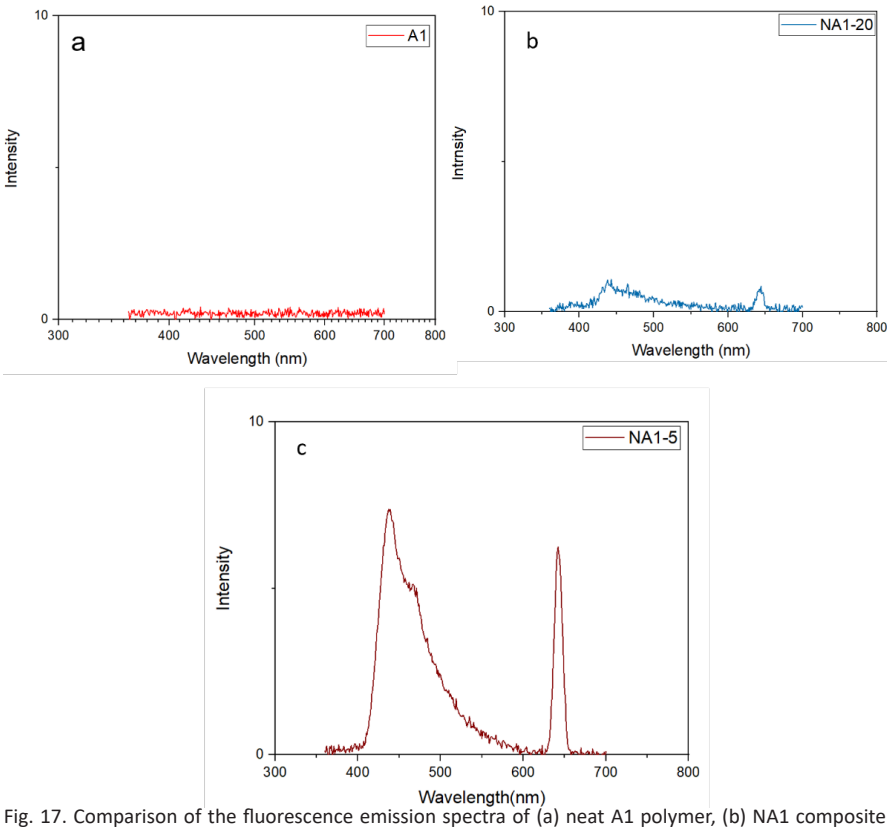


Fig. 17. Comparison of the fluorescence emission spectra of (a) neat A1 polymer, (b) NA1 composite containing 20-min carbon, and (c) NA1 composite containing 2wt% of 5-min carbon.

particle–particle contact and aggregation within the polymer matrix, thereby promoting non-radiative relaxation pathways and fluorescence quenching. In addition, the longer carbonization time of 20 min may result in a higher degree of carbonization and a relative reduction in the number or effectiveness of emissive surface states.

In contrast, the newly prepared composite containing 2 wt% of the yellow carbon material prepared for 5 min exhibited a pronounced increase in fluorescence intensity, with a broad emission band centered approximately around 450 nm. This enhancement can be related to the significantly lower carbon loading compared with the previous 1:1 composite, which may reduce aggregation and improve particle dispersion within the polymer matrix. Moreover, the shorter preparation time may preserve a larger population of optically active surface states and functional groups that contribute to the emission process. These results therefore suggest that the fluorescence behavior of the prepared composites is strongly influenced by both the degree of carbonization and the carbon loading level within the polymer matrix [35,36].

*UV-VIS Analysis*

As shown in Fig. 18, the UV–Vis absorption behavior was strongly influenced by the carbon preparation time, reflecting changes in both the carbonized domains and surface electronic states. The spectra of cellulose and the carbon samples prepared at different treatment times (Fig. 18a) show progressive changes in the absorption profile with increasing treatment time, which can be associated with the gradual conversion of the cellulose precursor into carbonized structures. During the early stages of carbonization, dehydration and condensation lead to the formation of small carbon nuclei while a considerable fraction of oxygen-containing functional groups, such as hydroxyl, carbonyl, and C–O-containing groups, remains at the particle surface. With prolonged treatment, further condensation and carbonization promote the development of larger or more extended conjugated $sp^2$ carbon domains, accompanied by modification or partial loss of some oxygen-containing surface functionalities.

This structural evolution is also reflected in the absorption behavior of the corresponding A1-based

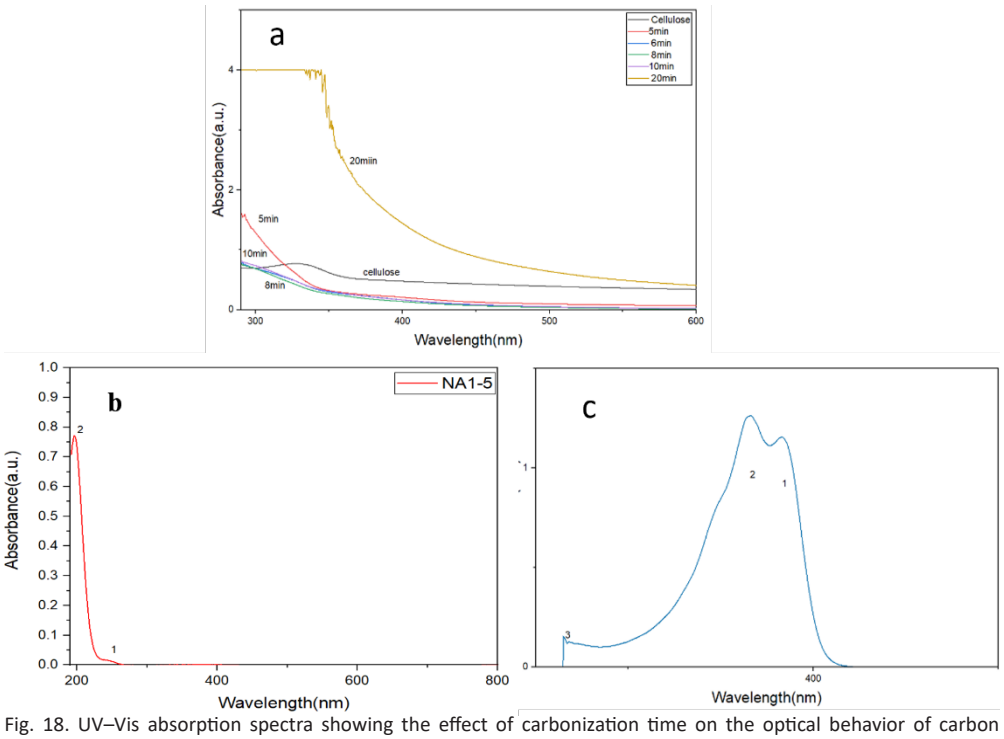


Fig. 18. UV–Vis absorption spectra showing the effect of carbonization time on the optical behavior of carbon materials and A1-based carbon/polymer composites: (a) cellulose and carbon samples prepared at different treatment times, (b) NA1-5 composite, and (c) NA1-20 composite.

composites. The composite containing carbon prepared for 5 min (NA1-5, Fig. 18b) exhibited a dominant absorption band at approximately 196 nm, which can be mainly associated with high-energy π→π* transitions involving unsaturated and aromatic/conjugated structures. In contrast, the composite containing carbon prepared for 20 min (NA1-20, Fig. 18c) exhibited an absorption feature at approximately 265 nm, attributed predominantly to π→π* transitions within conjugated C=C/sp² carbon domains, together with distinct bands at approximately 366 and 383 nm. The latter absorption features can involve n→π* transitions associated with oxygen-containing groups, particularly carbonyl C=O functionalities, as well as electronic transitions involving surface states and extended conjugated domains. Thus, the longer-wavelength absorption observed for NA1-20 is consistent with modification of the electronic structure and further development of conjugated carbon domains as the treatment time increases [37,38].

Importantly, the optical behavior of carbon dots cannot be described by assigning absorption exclusively to the carbon core and fluorescence exclusively to surface functional groups. Both components contribute to the electronic absorption process: the conjugated sp² carbon core primarily provides π-electronic states responsible for π→π* transitions, whereas oxygen-containing surface groups and surface defects introduce additional electronic states that can participate in n→π* transitions and generate surface-related energy levels. Following photoexcitation, these surface states may provide radiative recombination pathways responsible for fluorescence; however, the absorbed energy may alternatively undergo non-radiative relaxation. Therefore, increased carbonization and extended conjugation can enhance or shift optical absorption without necessarily producing stronger fluorescence. The spectral differences observed in Figs. 18a–c, together with the previous FT-IR results, consequently indicate that treatment time controls the balance between carbon-core development and surface functionalization, which in turn governs the absorption and fluorescence behavior of the resulting carbon/polymer composites [39,40].

*Thermogravimetric Analysis (TGA).*

Fig. 19 presents the thermogravimetric and

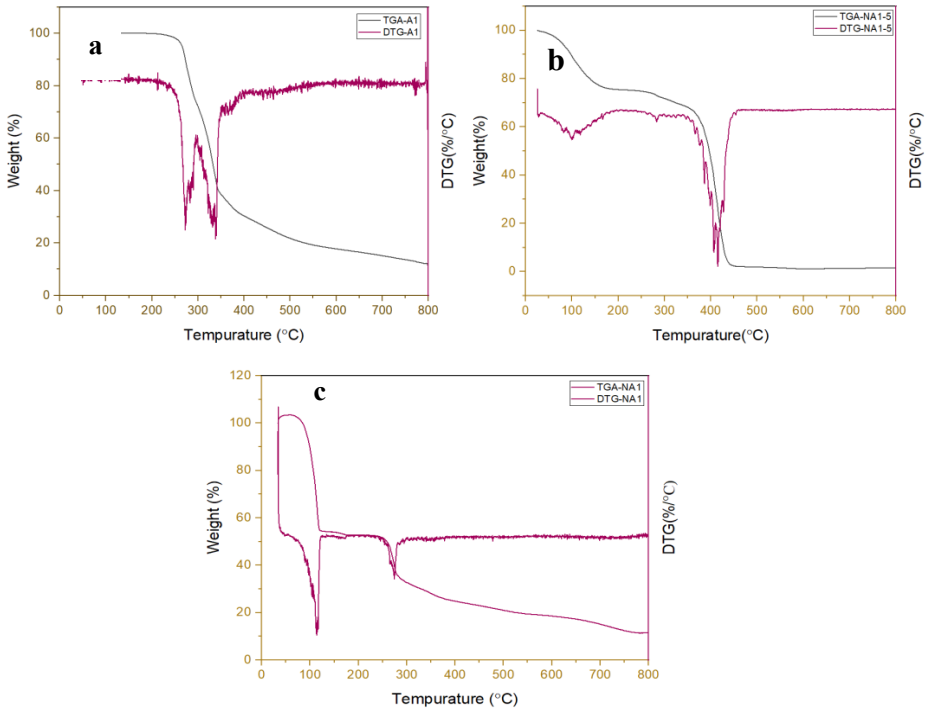


Fig. 19. TGA and DTG thermograms of (a) neat A1 polymer, (b) NA1-5 composite containing carbon dots prepared at 5 min, and (c) NA1-20 composite containing carbon dots prepared at 20 min.

derivative thermogravimetric (TGA/DTG) curves of the neat A1 polymer and its composites prepared using carbon samples obtained at two different treatment times, in order to evaluate the influence of carbon preparation time on the thermal degradation behavior of the polymer matrix. The neat A1 polymer (Fig. 19a) exhibited a weight loss of 25.84% within the temperature range of 34.87–295 °C, followed by the main decomposition stage between 295 and 430 °C, with a weight loss of 46.52%, and an additional weight loss of 15.48% up to approximately 799 °C. The corresponding DTG profile also indicates that the highest rates of mass loss are mainly concentrated within the thermal decomposition region of the polymer matrix.

Upon incorporation of the carbon sample prepared for 5 min, the NA1-5 composite (Fig. 19b) exhibited a noticeable change in its thermal degradation pattern. Weight losses of 10.70% and 13.95% were observed within 25.75–100 °C and 100–210 °C, respectively, followed by a weight loss of 28.86% between 210 and 400 °C. In contrast, the largest mass-loss stage, accounting for 43.19%, occurred within the higher temperature range of 400–440 °C and was accompanied by a pronounced DTG signal in the same region. The shift of the major mass-loss stage toward higher temperatures compared with the neat A1 polymer indicates a delay in the principal degradation stage of the polymer matrix following the incorporation of the carbon sample prepared for 5 min. This behavior may be associated with interfacial interactions between the surface functional groups of the carbon particles and the polar groups of the polymer chains, thereby influencing the thermal degradation pathway.

In contrast, the composite containing carbon prepared for 20 min, NA1-20 (Fig. 19c), displayed markedly different thermal behavior. A substantial weight loss of 45.19% occurred within 33.75–120 °C, followed by losses of 15.78% between 120 and 275 °C, 19.80% within 275–560 °C, and 7.60% between 560 and 800 °C. The sharp initial decrease in the TGA curve is consistent with the strong DTG signal observed in the low-temperature region. Since a mass loss of approximately 45% below 120 °C is unusually high to be attributed solely to structural degradation of the polymer, this stage may be associated with the presence of volatile components, moisture, and/or weakly bound species within the sample and therefore cannot be assigned entirely to degradation of the polymer chains.

Overall, comparison of Figs. 19a–c demonstrates that changing the carbon preparation time resulted in a pronounced difference in the thermal degradation patterns of the composites. NA1-5 showed a shift of its major mass-loss stage toward a higher temperature range compared with A1, whereas NA1-20 was characterized by substantial mass loss at relatively low temperatures. These differences may be related to variations in the degree of carbonization, surface chemistry, and surface functional groups of the carbon samples resulting from different treatment times, consistent with the FT-IR results, which revealed differences in the surface functionalities of the carbon samples prepared at 5 and 20 min. Collectively, these findings indicate that the preparation time of the carbon particles is an important factor governing their interaction with the polymer matrix and, consequently, the thermal degradation pathway of the resulting composite [41].

## CONCLUSION

The A1–A3 polyamide polymers and their corresponding carbon-based composites were successfully prepared and characterized using FT-IR, ^1H NMR, ^13C NMR, XRD, FESEM, TEM, EDX, UV–Vis, fluorescence, and TGA analyses. The results demonstrated that the properties of the carbonaceous nanomaterial were strongly dependent on the preparation time. Short treatment (5 min) produced a less carbonized material enriched in oxygen- and nitrogen-containing surface species and exhibiting noticeable fluorescence, whereas prolonged treatment (20 min) resulted in a more carbon-rich and highly carbonized structure with markedly reduced fluorescence. FT-IR, EDX, and FESEM analyses collectively supported the evolution of surface chemistry and morphology with increasing treatment time. Importantly, the composite containing the 5-min carbonaceous material retained detectable fluorescence, while the composite prepared using the 20-min material showed pronounced fluorescence quenching. The thermal behavior of the composites was also dependent on the nature and dispersion of the carbonaceous phase rather than showing a uniform improvement after its incorporation. Overall, these findings demonstrate that the performance of carbon-based polyamide composites is governed

not simply by the presence of the nanocarbon filler, but by controlling its carbonization degree, surface chemistry, aggregation, and dispersion within the polymer matrix. Therefore, controlling the preparation conditions of the carbonaceous nanomaterial is a critical step toward obtaining polymer composites with tunable optical and thermal properties.

## CONFLICT OF INTEREST

The authors declare that there is no conflict of interests regarding the publication of this manuscript.

## REFERENCES


1. Hirschberg V, Rodrigue D. Recycling of polyamides: Processes and conditions. J Polym Sci. 2023;61(17):1937-1958.
2. Winnacker M. Polyamides Derived from Terpenes: Advances in Their Synthesis, Characterization and Applications. Eur J Lipid Sci Technol. 2023;125(5).
3. Gonzalez de Gortari M, Misra M, Mohanty AK. Polyphthalamide polymers: A review on synthesis, properties, and advance manufacturing and emerging applications. J Appl Polym Sci. 2022;139(40).
4. Varghese M, Grinstaff MW. Beyond nylon 6: polyamides via ring opening polymerization of designer lactam monomers for biomedical applications. Chem Soc Rev. 2022;51(19):8258-8275.
5. Zhang Z, Fan K, Liu Y, Xia S. A review on polyester and polyester-amide thin film composite nanofiltration membranes: Synthesis, characteristics and applications. Sci Total Environ. 2023;858:159922.
6. Ramakoti IS, Panda AK, Gouda N. A brief review on polymer nanocomposites: current trends and prospects. J Polym Eng. 2023;43(8):651-679.
7. Khan I, Khan I, Saeed K, Ali N, Zada N, Khan A, et al. Polymer nanocomposites: an overview. Smart Polymer Nanocomposites: Elsevier; 2023. p. 167-184. http://dx.doi.org/10.1016/b978-0-323-91611-0.00017-7
8. Kar DK, V P, Si S, Panigrahi H, Mishra S. Carbon Dots and Their Polymeric Nanocomposites: Insight into Their Synthesis, Photoluminescence Mechanisms, and Recent Trends in Sensing Applications. ACS Omega. 2024;9(10):11050-11080.
9. Liu H, Zhong X, Pan Q, Zhang Y, Deng W, Zou G, et al. A review of carbon dots in synthesis strategy. Coord Chem Rev. 2024;498:215468.
10. Li H, Kang Z, Liu Y, Lee S-T. Carbon nanodots: synthesis, properties and applications. J Mater Chem. 2012;22(46):24230.
11. Pandey M, Pradhan N, Abu Elella MH, Makhado E, Samy M, Botlhoko OJ, et al. Frontiers in polymer/carbon dots nanocomposites: Recent advances in synthesis and diverse applications. Surfaces and Interfaces. 2025;60:106101.
12. Zainab Hassan R, Nadia Sadiq M. Synthesis and Characterization of some new heterocyclic derivatives from terphthaldehyde and study of their biological activity. Journal of Kufa for Chemical Sciences. 2023;3(1):223-239.
13. Yakan H. Preparation, structure elucidation, and antioxidant activity of new bis(thiosemicarbazone) derivatives. Turkish Journal of Chemistry. 2020;44(4):1085-1099.
14. Gavali LV, Mohammed AA, Al-Ogaili MJK, Gaikwad SH, Kulkarni M, Das R, et al. Novel terephthalaldehyde bis(thiosemicarbazone) Schiff base ligand and its transition metal complexes as antibacterial Agents: Synthesis, characterization and biological investigations. Results in Chemistry. 2024;7:101316.
15. Abbasi H, Antunes M, Velasco JI. Recent advances in carbon-based polymer nanocomposites for electromagnetic interference shielding. Prog Mater Sci. 2019;103:319-373.
16. Spectroscopic study on Thiourea and Thiosemicarbazide in Nonaqueous media. IOSR Journal of Applied Physics. 2013;4(1):05-08.
17. Ali SAM, Salem ME, Ibrahim AZ, Mahmoud MAA, Abdel-Megid M, Hussein BHM. Retracted Article: Novel thiosemicarbazone UV-vis chemosensor for dual pH-orthogonal detection of Fe3+ and Ag+. RSC Advances. 2026;16(5):3850-3867.
18. Ghaemy M, Mighani H, Alizadeh R. Synthesis and characterization of Schiff-base-containing polyamides. Chin J Polym Sci. 2010;29(2):149-155.
19. Huang H, Ge H, Ren Z, Huang Z, Xu M, Wang X. Controllable Synthesis of Biocompatible Fluorescent Carbon Dots From Cellulose Hydrogel for the Specific Detection of $Hg^{2+}$. Frontiers in Bioengineering and Biotechnology. 2021;9.
20. Fan J, Kang L, Gao J, Cheng X, Zhang Q, Wu Y. Preparation of Microcrystalline Cellulose-Derived Carbon Dots as a Sensor for Fe3+ Detection. Coatings. 2023;13(12):1979.
21. Marpongahtun M, Andriayani A, Muis Y, Gea S, Amaturrahim SA, Attaurrazaq B, et al. Synthesis of Nitrogen-Doped Carbon Dots from Nanocrystalline Cellulose by Pyrolysis Method as $Hg^{2+}$ Detector. International Journal of Technology. 2023;14(1):219.
22. Rosell M, Torregrosa-Rivero V, Herrera-Ochoa D, Garzón-Ruiz A, García-Martínez J, Serrano E, et al. Unlocking the Potential of Different Types of Biomass-Derived Carbon Dots as Fluorescence Lifetime Imaging Probes. ChemPhotoChem. 2024;8(10).
23. Shirke YM, Abou-Elanwar AM, Choi W-K, Lee H, Hong SU, Lee HK, et al. Influence of nitrogen/phosphorus-doped carbon dots on polyamide thin film membranes for water vapor/$N_2$ mixture gas separation. RSC Advances. 2019;9(55):32121-32129.
24. Sheshmani S, Mardali M, Shokrollahzadeh S, Bide Y, Tarlani R. Synthesis, optical, and photocatalytic properties of cellulose-derived carbon quantum dots. Sci Rep. 2025;15(1).
25. Eddy NO, UdeokpoteEngr GC, Dinneya-Onuoha E, Garg R, Garg R, Paktin H. Synthesis of carbon quantum dots using unutilized low-grade lignite coal. BMC Chemistry. 2026;20(1).
26. Alamdari NG, Almasi H, Moradi M, Akhgari M. Characterization of Carbon Quantum Dots Synthesized from Vinasse and Date Seeds as Agro-industrial Wastes. Waste and Biomass Valorization. 2023;14(11):3689-3703.
27. Ozyurt D, Kobaisi MA, Hocking RK, Fox B. Properties, synthesis, and applications of carbon dots: A review. Carbon Trends. 2023;12:100276.
28. Aziz SB, Abdullah OG, Brza MA, Azawy AK, Tahir DA. Effect of carbon nano-dots (CNDs) on structural and optical properties of PMMA polymer composite. Results in Physics. 2019;15:102776.
29. Ru Y, Waterhouse GIN, Lu S. Aggregation in carbon dots.

Aggregate. 2022;3(6).
30. Adsetts JR, Hoesterey S, Gao C, Love DA, Ding Z. Electrochemiluminescence and Photoluminescence of Carbon Quantum Dots Controlled by Aggregation-Induced Emission, Aggregation-Caused Quenching, and Interfacial Reactions. Langmuir. 2020;36(47):14432-14442.
31. Conquering Aggregation-Induced Solid-State Luminescence Quenching of Carbon Dots through a Carbon Dots-Triggered Silica Gelation Process. American Chemical Society (ACS).
32. Elugoke SE, Uwaya GE, Quadri TW, Ebenso EE. Carbon Quantum Dots: Basics, Properties, and Fundamentals. ACS Symposium Series: American Chemical Society; 2024. p. 3-42.
33. Chen S, Guo Q, Yu J. Bio-inspired functional coacervates. Aggregate. 2022;3(6).
34. Papaioannou N, Titirici M-M, Sapelkin A. Investigating the Effect of Reaction Time on Carbon Dot Formation, Structure, and Optical Properties. ACS Omega. 2019;4(26):21658-21665.
35. Yoo HJ, Kwak BE, Kim DH. Competition of the roles of π-conjugated domain between emission center and quenching origin in the photoluminescence of carbon dots depending on the interparticle separation. Carbon. 2021;183:560-570.
36. Wang J, Yang Y, Liu X. Solid-state fluorescent carbon dots: quenching resistance strategies, high quantum efficiency control, multicolor tuning, and applications. Materials Advances. 2020;1(9):3122-3142.
37. Wang Z, Changotra R, Dong G, Yang J, He QS. Cellulose carbon quantum dots decorated CdS nanocatalyst for enhanced visible-light photocatalytic hydrogen evolution. Sustainable Carbon Materials. 2026;2(1).
38. Lee W, Ko S. Synthesis and Characterization of Lignocellulose-Based Carbon Quantum Dots (CQDs) and Their Antimicrobial and Antioxidant Functionalities. Molecules. 2025;30(3):667.
39. Roy AK, Humayun AB, Acharjee Y-r, Usha NJ, Majumder S. Carbon quantum dot-based thin films for multifunctional and sustainable applications. Materials Advances. 2026;7(10):4943-4972.
40. Jlassi K. Rational Synthesis, Characterization, and Application of Environmentally-Friendly (Polymer-Carbon Dot) Hybrid Composite Film for Fast and Efficient UV Assisted $Cd^{2+}$ removal from water. University of the Future: Re-Imagining Research and Higher Education; 2020/10/28: Qatar University Press; 2020. p. 66.
41. Carbon Nanotubes-Reinforced Thermoplastic Nanocomposites. Recent Advances in Polymer Nanocomposites: Synthesis and Characterisation: CRC Press; 2010. p. 197-220.